Supporting Information

Peng et al. 10.1073/pnas.1007524107

SI Text

Materials and Methods. ***Chemicals.*** Silver nitrate ($AgNO_3$, 99.9999% trace metals basis), oleylamine (OAm, technical grade, 70%), oleic acid (OA, technical grade, 90%), acetone (Fluka, purum, ≥99.0%), toluene (CHROMASOLV, ≥99.9%), chloroform ($CHCl_3$, CHROMASOLV Plus, ≥99.9%, contains amylenes as stabilizer), and 1-hexadecanethiol (HDT, technical grade, 92%) were purchased from Sigma-Aldrich. Hexane (Mallinckrodt, AR*ACS Grade) and nitric acid (HNO_3, ACS grade, 68.0–70.0%, EMD) were purchased from VWR International. All chemicals were used as received without any further purification.

Synthesis and Purification of Ag Nanoparticles (NPs). The typical synthesis of Ag NPs with size of 10.0 nm has been described in the *Materials and Methods* section in the paper. It is noteworthy that the reaction mixture was colorless and transparent until 140 °C and started to become dark at higher temperatures, indicating the formation of Ag nanoclusters (i.e., nucleation process). The final product was a dark brown dispersion. The cooled dispersion was then mixed with 40 ml acetone and centrifuged at ~8500 rpm for 8 min (using a Beckman Coulter Avanti J-E Centrifuge). The light-brownish supernatant was decanted and the precipitated Ag NPs were then redispersed in 10 ml hexane. The washing process was repeated one more time before the Ag NPs were dispersed in hexane and stored in a 20 ml scintillation vial. For the purpose of long-term storage, 0.05 ml fresh OAm was added to the hexane dispersion. The nucleation and growth of Ag NPs have been monitored by taking hot aliquots (~0.5 ml) out at different reaction stages followed by quenching the reaction in an ice-water bath. The cooled aliquots were then washed accordingly and the nanoparticles were characterized with TEM.

To remove the fraction of smaller NPs in the as-prepared dispersions and achieve Ag NPs with narrow size distribution, size selection processes were carried out. Acetone was carefully added drop-by-drop to a hexane dispersion of concentrated Ag NPs (3–5 mg in 0.5 ml) in a 2 mL microtube until the dispersion just became turbid. Then the mixture was centrifuged at a rate of ~2,000–6,000 rpm for 5 min (using a VWR microcentrifuge Galaxy 14D centrifuge). The light-brownish supernatant was carefully decanted and hexane was added to the microtube to redisperse the precipitated Ag NPs. Such process was repeated one or two more times.

Syntheses of Ag NPs with different sizes were carried out by varying the reaction conditions. The amounts of $AgNO_3$ and OAm in each synthesis were kept the same. Ag NPs with diameters ranging from ~7 nm to ~18 nm were successfully synthesized by changing the reaction temperature. For example, Ag NPs with diameter of 7.3 nm were obtained by lowering the reaction temperature to 140 °C, while the reactions at 210 °C, 240 °C, and 270 °C produced Ag NPs of 12.5 nm, 15.6 nm, and 17.8 nm, respectively. It is noteworthy that for reactions carried out at 240 °C and 270 °C, Ag NP suspensions rather than dispersions resulted probably due to the drastic increase of the NP overall density (according to size increase) and thus the insufficient repulsive dispersing force to support them in the solution. However, these suspensions are stable for UV-Vis experiments and no agglomeration of NPs was observed during the measurements. Unfortunately, with the current synthetic strategy, attempts to synthesize monodispersed Ag NPs larger than 20 nm were unsuccessful because of serious and irreversible aggregations during syntheses at high temperatures, i.e. 300 °C, which resulted in mirror-like unsuspended precipitations. Smaller Ag NPs with d of 2–5 nm were synthesized with addition of trace amounts of oleic acid (OA), which has the same hydrocarbon chain structure as OAm, to the reaction system because the carboxylic group of OA can strongly bond Ag^+ ions to prevent fast growth of Ag NPs. For example, addition of 0.1 ml OA to the initial reaction mixture, while keeping the reaction temperature (180 °C) and the reaction time (1 hr) the same, led to the formation of Ag NPs with diameters of 4.7 nm. On the other hand, a reaction with the presence of 0.5 ml OA at 180 °C gave 3.3-nm Ag NPs. Given that the amount of OA is much less than that of OAm in the reaction system, the Ag NPs are protected essentially with a layer of pure OAm. For reactions at the same temperature, addition of more OA resulted in smaller Ag NPs. The reaction time also played a role on the particle size, i.e., lengthening the reaction time slightly enlarged the NPs. For example, lengthening a 4.7-nm Ag NP synthesis (0.1 ml OA, 180 °C, 1 hr) to 2 hrs led to the formation of 5.3-nm Ag NPs, while extending a 3.3-nm Ag NP synthesis (0.5 ml OA, 180 °C, 1 hr) to 2 hrs gave 3.9-nm Ag NPs. The synthesis of 2.2-nm Ag NPs was carried out with the presence of 0.5 ml OA and the reaction was maintained at 120 °C for 2 hrs.

Characterizations. Samples for transmission electron microscopy (TEM) analysis were prepared by putting droplets of a dilute dispersion of the Ag NPs on amorphous carbon-coated copper grids, which were purchased from Ted Pella. The samples were then dried in a fume hood at room temperature. TEM images were taken on a Philips CM30 with an acceleration voltage of 200 kV. High resolution TEM (HRTEM) images were recorded using a JEOL 2010F microscope with an acceleration voltage of 200 kV. High-angle annular dark field scanning TEM (HAADF-STEM) images were recorded using a JEOL 2200FS (S)TEM microscope with an acceleration voltage of 200 kV and STEM mode. UV/Vis absorption spectra and Fourier transform infrared (FTIR) spectra were collected on a Perkin Elmer Lambda 950 spectrometer and a Bruker Vertex 70 spectrometer, respectively.

Quantitative Measurements of UV-Vis Absorption Spectra and Concentrations of Ag NPs. Quantitative measurements of the UV-Vis absorption spectra of Ag NPs of various sizes have been described in the *Materials and Methods* section in the paper. All spectra were measured multiple times on multiple batches of samples right after the synthesis and after storage for weeks to eliminate the influence of aging. The results showed that the synthesized Ag NPs capped with OAm molecules were very stable and no detectable variation of their absorption spectra were observed even after long-time storage in ambient environment. Inductively coupled plasma optical emission spectroscopy (ICP-OES) was used to measure the precise concentrations of Ag in dispersions. All the measurements were carried out with a PerkinElmer Optima 2100 DV ICP-OES system. In a typical measurement, 200 μl of Ag NP hexane dispersion (2.0 mg/ml) mentioned above was first added to a scintillation vial and dried under N_2. 1 ml of concentrated nitric acid (HNO_3) was then added to destroy and dissolve the Ag NPs. The vial was heated on a hotplate setting at 80 °C for about 3 min to facilitate complete dissolution of the Ag NPs. Addition of 4 ml of deionized (DI) water to the vial followed by gentle shaking finished the sample preparation. This solution was further diluted two times before actual ICP-OES measurements. The results were used to calculate the numbers of Ag NPs in a 1 ml dispersion. The detailed particle size, particle

concentration, and absorption cross section are summarized in Table S1.

Surface Ligand Exchange. The procedure for surface ligand exchange using HDT molecules has been described in detail in the *Materials and Methods* section in the paper. It is noteworthy that for each sample of Ag NPs of different size, the whole set of measurements was completed within 1 hr. The concentrations of HDT ([HDT], μM) and the absorbance of the measured UV-Vis spectra were normalized according to the total volume of the solution in the cuvette.

Stability of Ag NPs Under Air and at Elevated Temperature. In a typical test, 2.0 mg of 5.3-nm Ag NPs were dried under N_2 and quickly redispersed in 10 ml toluene with the presence of 0.1 mmol OAm (~34 μl). Compressed air with a flow rate of ~200 cm^3/min was bubbled beneath the solution surface using a stainless steel needle for 10 min at room temperature before the mixture was heated up to 70 °C. The dispersion was maintained at 70 °C for 24 hr as the air was continuously bubbled. Aliquots (~0.1 ml) were taken out at various times, and UV-Vis spectra were monitored.

Theoretical Model. We calculated the optical properties using analytical, multilayer Mie theory (1, 2) and the structure depicted in Fig. 3*B* of the main text. The structure involves (*i*) a central spherical metal core of radius $r_c = d/2 - t$, (*ii*) a surrounding shell from radii r_c to $r_c + t = d/2$ corresponding to the reduced conductivity layer, (*iii*) a shell corresponding to the surfactant layer from radii $d/2$ to $d/2 + s$, and finally (*iv*) the relevant solvent surrounding the particle-surfactant complex for radii greater than $d/2 + s$. For region *i* we employ the bulk Ag dielectric constant (3). For region *ii* we break down the dielectric constant into interband and intraband terms, describe the intraband term with a Drude model, and reduce the conductivity of the region by lowering the plasma frequency by a factor *g*. Finally, standard values for the dielectric constants of the surfactant and solvent are employed. We fix *t* to be roughly the thickness of an atomic Ag layer, $t = 0.25$ nm. The surfactant thickness layer was taken to be $s = 2$ nm for OAm and $s = 1.8$ nm for HDT. Optimal values of *g*, based on comparison with the experimental results, were 0.795 and 0.74 for the OAm and HDT surfactants, respectively.

Regarding the other dielectric constants, they are given by n^2, where *n* are the bulk refractive indices: $n = 1.375$, 1.446, and 1.496 for the hexane, chloroform, and toluene solvents, and $n = 1.4596$ and 1.462 for OAm and HDT surfactants. The bulk, wavelength or frequency- dependent relative dielectric constant for bulk Ag, $\varepsilon(\omega)$, was taken from the experimental data for silver (3). We reexpress $\varepsilon(\omega)$ in terms of interband and intraband contributions,

$$\varepsilon(\omega) = \varepsilon_{\text{inter}}(\omega) + \varepsilon_{\text{intra}}(\omega,\omega_D,\gamma_D) \qquad \textbf{[S1]}$$

with

$$\varepsilon_{\text{inter}}(\omega) = \varepsilon(\omega) - \varepsilon_{\text{intra}}(\omega,\omega_p,\gamma_p) \qquad \textbf{[S2]}$$

The intraband term that is subtracted off the full bulk dielectric constant in Eq. **S2** is given by

$$\varepsilon_{\text{intra}}(\omega,\omega_p,\gamma_p) = 1 - \frac{\omega_p^2}{\omega^2 + i\gamma_p\omega}. \qquad \textbf{[S3]}$$

A fit of Eq. **S3** to the bulk data in the $\lambda = 500$–1000 nm range yields $\hbar\omega_p = 8.775$ eV and $\hbar\gamma_p = 0.02$ eV. To allow for the possibility of both a lowered conductivity and/or interfacial scattering effects, the intraband term that is ultimately added to the interband term of Eq. **S2** will be a Drude form with possibly different plasma parameters,

$$\varepsilon_{\text{intra}}(\omega,\omega_D,\gamma_D) = 1 - \frac{\omega_D^2}{\omega^2 + i\gamma_D\omega}. \qquad \textbf{[S4]}$$

Note that in the Drude model the carrier density, and thus conductivity, is proportional to the square of ω_D in Eq. **S4**. By choosing

$$\omega_D = g\omega_p, \qquad \textbf{[S5]}$$

with the magnitude of *g* less than one we effectively lower the conductivity.

For the case of no interfacial damping correction, the $\varepsilon(\omega)$ values from ref. 3 are directly employed for the inner metallic core. In the lower-conductivity layer of thickness *t*, we employ Eq. **S1** with $\gamma_D = \gamma_p$.

Size-dependent, interfacial damping is introduced by taking (1, 4)

$$\gamma_D = \gamma_p + \frac{Av_F}{r}, \qquad \textbf{[S6]}$$

with Fermi velocity $v_F = 1.4 \times 10^6$ m/s, $A = 1$, and $r = d/2$. The core region is then described by Eq. **S1** with the intraband term, Eq. **S4**, having $g = 1$ to define ω_D but γ_p replaced by γ_D of Eq. **S6**.

We should point out that the conductivity in question is the AC (or optical) conductivity, which within the Drude model is given by

$$\sigma_D(\omega) = \frac{\varepsilon_0\omega_D^2/\gamma_D}{1 - i\frac{\omega}{\gamma_D}}, \qquad \textbf{[S7]}$$

where the numerator on the right-hand side is the DC conductivity. Since it is the case that the optical frequencies we are interested in are such that $\omega \gg \gamma_D$, the imaginary part of the denominator can be quite large in magnitude and so the AC conductivity is very different in character from the static DC ($\omega = 0$) limit. The Drude relative dielectric constant is related to the AC conductivity via

$$\varepsilon_D(\omega) = 1 + i\frac{\sigma_D(\omega)}{\varepsilon_0\omega}. \qquad \textbf{[S8]}$$

This implies that by lowering the carrier density (proportional to ω_D^2), we are lowering the magnitude of both the real and imaginary parts of ε_D. This means that $\text{Re}(\varepsilon_D)$ becomes less negative, and it is this feature that is the key to obtaining the red-shift in SPR positions as particle size decreases. The SPR positions are very sensitive to changes in the magnitude of $\text{Re}(\varepsilon_D)$. The decrease in $\text{Im}(\varepsilon_D)$ leads to a slight narrowing of the resonance features, but this is not at all as significant of an effect. We should also note that Eqs. **S7** and **S8** also imply that it is $\text{Im}(\sigma_D)$ that is responsible for the decrease in the magnitude of $\text{Re}(\varepsilon_D)$ and thus the main effect.

When one considers the interfacial scattering correction, i.e., increases γ_D, it also affects the conductivity. However, it is easy to see, that in the limit of $\omega \gg \gamma_D$, which is still reasonable, that this correction increases $\text{Re}(\sigma_D)$, implying an increase in $\text{Im}(\varepsilon_D)$. There is only a small effect on $\text{Im}(\sigma_D)$ or $\text{Re}(\varepsilon_D)$. This correction therefore leads to a broadening of the SPR resonance and only slight shifts in its position for the frequencies or wavelengths studied here.

We should note that a three-layer model assuming a thin oxide layer instead of a reduced conductivity metallic layer can also lead to a reversal of the plasmon size-dependence. This is not surprising because the oxide layer also has reduced conductivity relative to the metallic core. We verified this by carrying out calculations using a 0.25 nm oxide layer with the experimentally determined, dispersive, complex Ag_2O refractive index (5). However, as detailed in the text and the previous section, special precautions were taken in our experiments to ensure that no oxidation occurred and additional experiments have confirmed that our particles are stable to resist oxidation.

Further Discussion on Ag NP morphology. Icosahedrons represent a class of platonic solids which are closest to spheres. In crystallography, an icosahedral NP has 20 {111} facets and contains 20 tetrahedral subunits joining along the twin boundaries (6). Such twinning feature is namely the multiple-twinned (MT) structure. One distinguishing morphological characteristic of the icosahedral MT NPs is the coexistence of three types of rotational axes: twofold, threefold, and fivefold ones, which can be used to differentiate from other frequently observed MT NPs, such as decahedrons (which also has fivefold MT structure but only with five tetrahedral subunit joining together). HRTEM studies (Fig. S2) revealed all three symmetries in Ag NPs of various sizes, thus confirming the icosahedral morphology.

The lattice fringe patterns, as shown in the HRTEM images, may not look exactly the same for the images with the same symmetry (e.g. Fig. 1*L* vs. Fig. S2 *F*, *I*, and *L* and Fig. S2*G* vs. Fig. S2*J*) because these images were not taken with the rotation axes perfectly parallel to the electron beam. It is reported that the TEM images are highly sensitive to disorientations and distortions of the icosahedron from its ideal structure (6). If an icosahedron is placed on a flat surface with its twofold, threefold, or fivefold rotation axes perpendicular to the surface, one of the edges, facets or vertices of the icosahedron would sit against the plane respectively, and threefold rotation axis is the most thermodynamically favorable case. In fact, observation of the twofold and fivefold symmetries is also possible in experiment because of the existence of the surfactant molecules and uneven surfaces of TEM grids. Fig. S2 *I* and *L* exhibit unique contrast patterns similar to quasicrystalline arrangement, revealing the existence of pentagonal motifs. In this case, the contrast is produced by the interference effect named "Moiré Pattern" which occurs when two or more crystalline planes overlap (6, 7). Such pattern is also helpful for distinguishing icosahedral NPs from decahedral NPs, both of which have fivefold MT structure. Our images greatly resemble the simulated and experimental images of icosaheral Au, Ag, and Fe NPs with fivefold symmetries (7–10).

To further confirm the structure of the NPs, fast Fourier transforms (FFT) were performed on the acquired HRTEM images. The FFT patterns shown in Fig. S2 *G–L* clearly show the twofold (*G* and *J*), threefold (*H* and *K*), and fivefold (*I* and *L*) symmetries, confirming that the nanoparticles with sizes of 7.3 nm and 5.3 nm have an icosahedral shape. If the nanoparticles were decahedral in shape, we would not be able to observe threefold symmetry.

In addition, theoretical calculations based on quenched molecular dynamics simulations concluded that the multiple-twinned icosahedral shape is the most favorable morphology of small Ag nanoparticles and that the multiple-twinned decahedral shape is favorable for the Ag nanoparticles with medium sizes (11). As clearly shown in Fig. 2 *D–F*, the 15.6-nm Ag nanoparticles have icosahedral shape. As shown in Fig. S2 *G–L*, we can also confirm that Ag nanoparticles with smaller sizes (<15 nm) are crystallized in an icosahedral morphology as well.

Overall, the as-synthesized Ag NPs with different sizes have the universal icosahedral morphology, which are confirmed by the coexistence of twofold, threefold, and fivefold symmetries for all the NPs. The consistency in particle morphology enables the elimination of the complication of size-dependent SPRs caused by shape-effect. However, due to the instrumental resolution limit, further detailed structural analyses cannot be performed. Interested readers can refer to more detailed and specialized studies (6–9).

1. Kreibig U, Genzel L (1985) Optical absorption of small metallic particles. *Surf Sci* 156:678–700.
2. Peña O, Pal U (2009) Scattering of electromagnetic radiation by a multilayered sphere. *Comput Phys Commun* 180:2348–2354.
3. Johnson PB, Christy RW (1972) Optical constants of the noble metals. *Phys Rev B* 6:4370–4379.
4. Coronado EA, Schatz GC (2003) Surface plasmon broadening for arbitrary shape nanoparticles: A geometrical probability approach. *J Chem Phys* 119:3926–3934.
5. Pettersson LAA, Snyder PG (1995) Preparation and characterization of oxidized silver thin films. *Thin Solid Films* 270:69–72.
6. Buffat P-A, Flüeli M, Spycher R, Stadelmann P, Borel J-P (1991) Crystallographic structure of small gold particles studied by high-resolution electron microscopy. *Faraday Discuss* 92:173–187.
7. Reyes-Gasga J, Tehuacanero-Nuñez S, Montejano-Carrizales JM, Gao X, Jose-Yacaman M (2007) Analysis of the contrast in icosahedral gold nanoparticles. *Top Catal* 46:23–30.
8. José Yacamán M, Ascencio JA, Liu HB, Gardea-Torresdey J (2001) Structure shape and stability of nanometric sized particles. *J Vac Sci Technol B* 19:1091–1103.
9. Ling T et al. (2009) Icosahedral face-centered cubic Fe nanoparticles: facile synthesis and characterization with aberration-corrected TEM. *Nano Lett* 9:1572–1576.
10. Harfenist SA, Wang ZL, Whetten RL, Vezmar I, Alvarez MM (1997) Three-dimensional hexagonal close-packed superlattice of passivated Ag nanocrystals. *Adv Mater* 9:817–822.
11. Baletto F, Ferrando R, Fortunelli A, Mottet C (2002) Crossover among structural motifs in transition and noble-metal clusters. *J Chem Phys* 116:3856–3863.
12. Leatherdale CA, Woo W-K, Mikulec FV, Bawendi MG (2002) On the absorption cross section of CdSe nanocrystal quantum dots. *J Phys Chem B* 106:7619–7622.

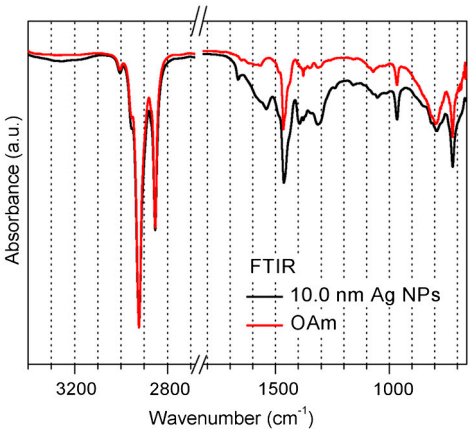

Fig. S1. FTIR spectra of pure OAm (red curve) and 10.0 nm-Ag NPs (black curve). The consistence in spectral features indicates that the synthesized Ag NPs are purely capped with OAm molecules.

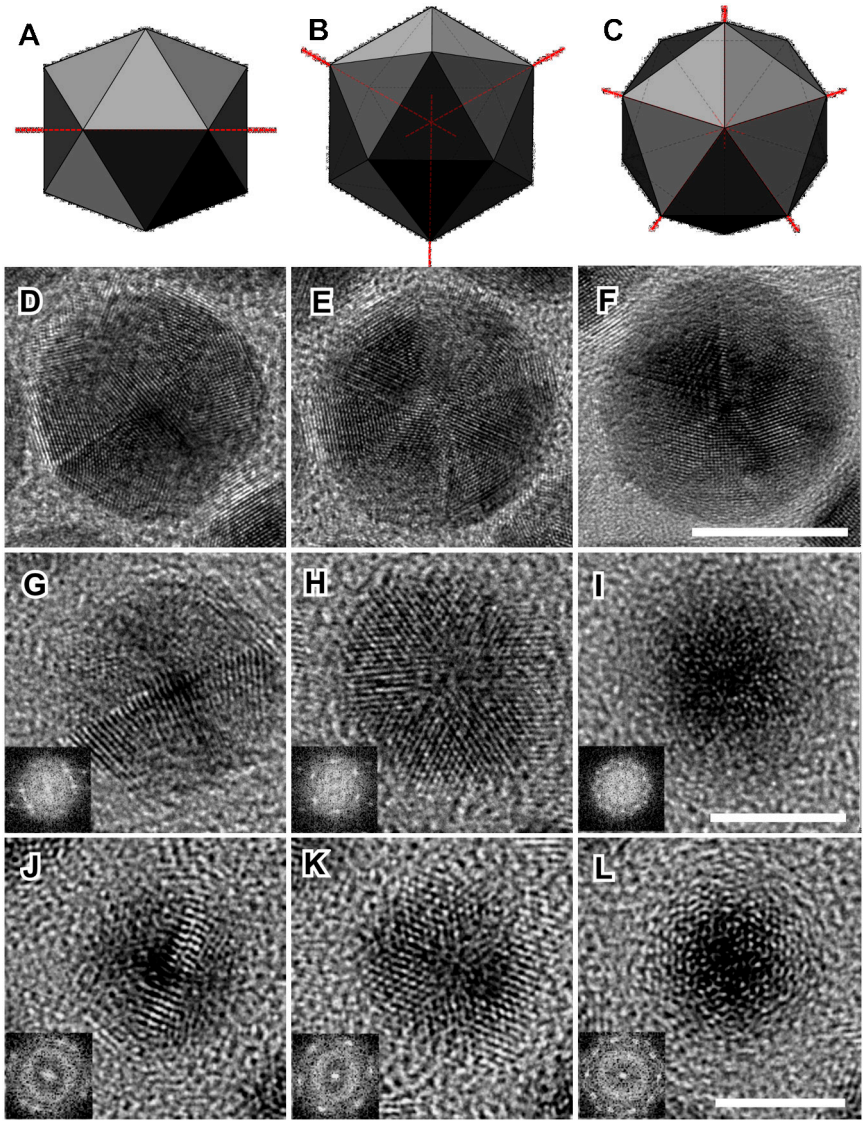

Fig. S2. Schematic drawings and HRTEM images of icosahedral Ag NPs of various sizes. (*A*–*C*) Schematic illustrations of an icosahedron viewed along its twofold (*A*), threefold (*B*) , and fivefold (*C*) rotation axes. The red dashed lines highlight the twin planes. HRTEM images of Ag NPs with diameter of (*D*–*F*) 15.6 nm, (*G*–*I*) 7.3 nm, and (*J*–*L*) 5.3 nm, which were obtained by aligning the electron beam along or close to the three rotation axes indicated in *A*–*C*. Scale bars in *F*, *I*, and *L* represent 10, 5, and 4 nm and apply to *D*–*F*, *G*–*I*, and *J*–*L*, respectively. Insets in *G*–*L* are fast Fourier transform patterns showing the symmetry of the nanoparticles.

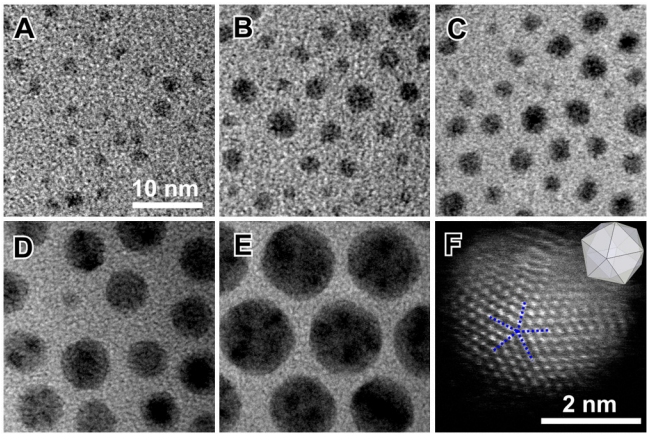

Fig. S3. TEM images of samples taken out at various stages of a typical synthesis of 10.0-nm Ag NPs: (*A*) 160 °C, (*B*) 180 °C 0 min, (*C*) 180 °C 2 min, (*D*) 180 °C 15 min, and (*E*) 180 °C 1 hr. The times are normalized to the time at which the temperature of the reaction mixture reached 180 °C. The scale bar in *A* applies for *A*–*E*. A high-angle annular dark field scanning TEM (HAADF-STEM) image (*F*) of an individual Ag NP (~4 nm) in *B* indicates the as-formed multitwinned structure at the initial stage of the reaction. Blue dotted lines highlight the fivefold multitwins, and the inset shows the corresponding orientation of the icosahedral NP. Careful analysis of the images reveals that all the nanocrystals, even those with very small sizes (i.e., the seeds shown in *A*) exhibit inhomogeneous contrast, indicating that they are multiple-twinned, not single-crystalline. The multiple-twinned crystalline structure of the seeds formed at the early reaction stage is consistent with that of the smaller Ag nanoparticles shown in Fig. 1. In addition, theoretical calculations based on quenched molecular dynamics simulations also concluded that multiple-twinned icosahedral shape is the most favorable morphology of small Ag nanoclusters (11). As a result, we can conclude that the monodisperse Ag nanoparticles synthesized in this work grow from multiple-twinned seeds rather than single-crystalline subunits.

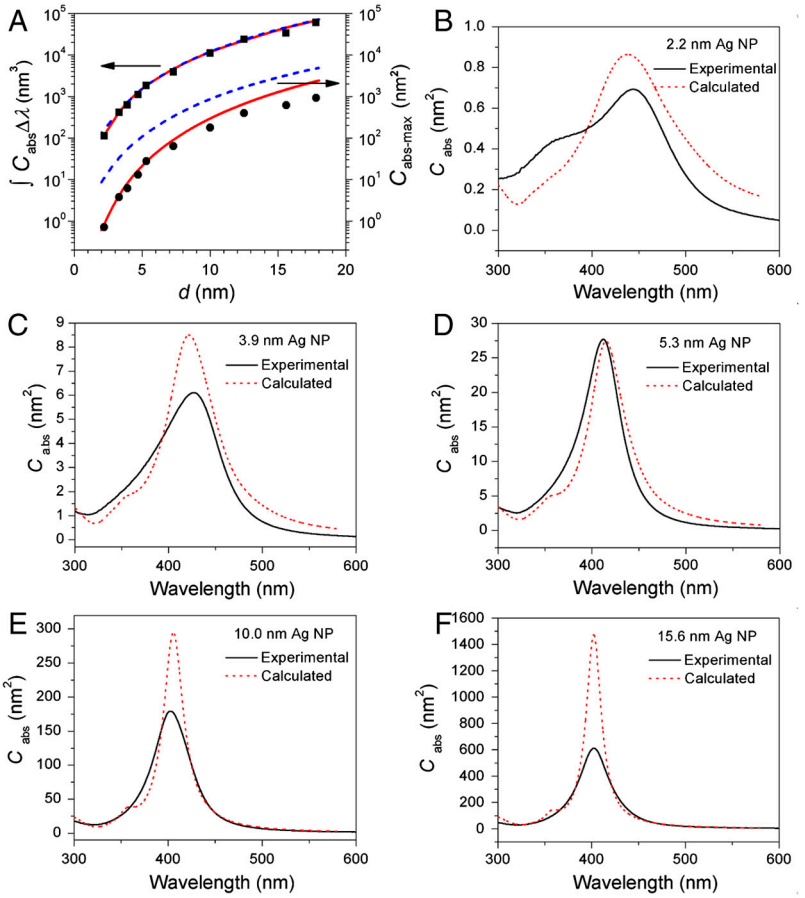

Fig. S4. Experimental and calculated absorption spectra of Ag NPs of various sizes. (*A*) Coplot of experimental (black symbols) and calculated (colored lines) absorption cross section integrated from 320 to 600 nm, $\int C_{abs}\Delta\lambda$ (nm^3) (left) and peak absorption cross section, $C_{abs\text{-}max}$ (nm^2) (right). Blue dashed lines represent calculated results without the inclusion of interfacial damping in the model, while red solid lines represent calculations with damping. (*B*–*F*) Representative coplots of experimental (solid black line) and calculated (red dotted line) absorption spectra of single Ag NPs with different diameters (*B*) 2.2 nm, (*C*) 3.9 nm, (*D*) 5.3 nm, (*E*) 10.0 nm, and (*F*) 15.6 nm.

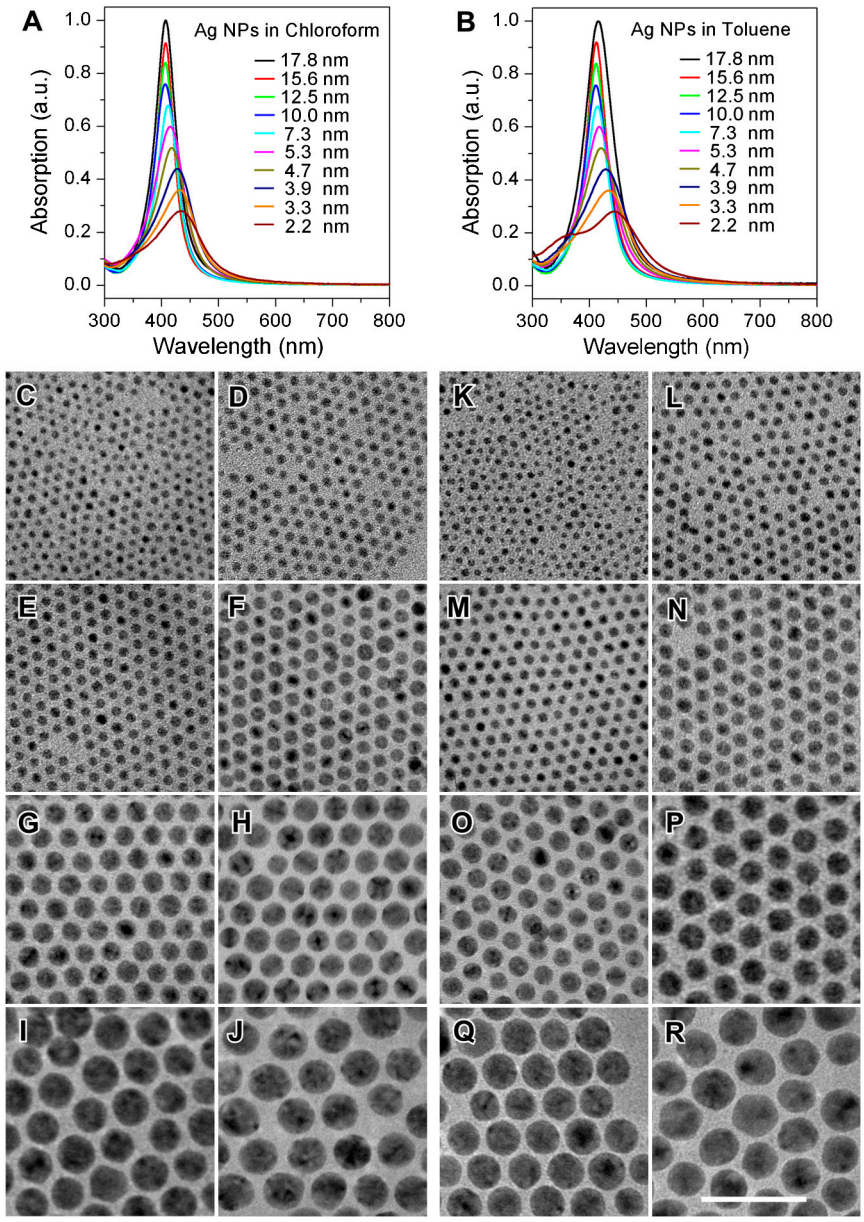

Fig. S5. Ag NPs dispersed in different media. UV-Vis absorption spectra of the Ag NPs of various sizes dispersed in Chloroform (*A*) and Toluene *B*). (While the relative peak height trends are correctly indicated, the spectra have been scaled in a manner similar to those presented in Fig. 2 for better clarity.) Representative TEM images of Ag NPs with different diameters: (*C*) (*K*) 3.3 nm, (*D*) (*L*) 3.9 nm, (*E*) (*M*) 5.3 nm, (*F*) (*N*) 7.3 nm, (*G*) (*O*) 10.0 nm, (*H*) (*P*) 12.5 nm, (*I*) (*Q*) 15.6 nm, and (*J*) (*R*) 17.8 nm. Panels (*C*–*J*) are from Ag NPs dispersed in chloroform while (*K*–*R*) are from those dispersed in toluene. Scale bar represents 50 nm and applies to all the TEM images.

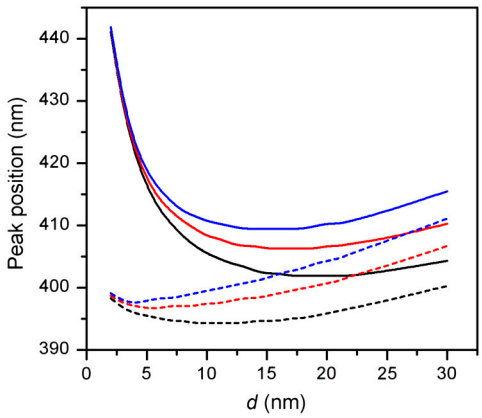

Fig. S6. Comparison of calculated SPR band positions including and excluding the modification of surface conductivity. Calculated size-dependent peak positions of Ag NPs dispersed in hexane, chloroform and toluene are represented in black, red, and blue, respectively. Solid lines represent calculations including the modification of surface conductivity, and dotted lines represent the ones without the modification. Both sets of calculations have included the interfacial damping term.

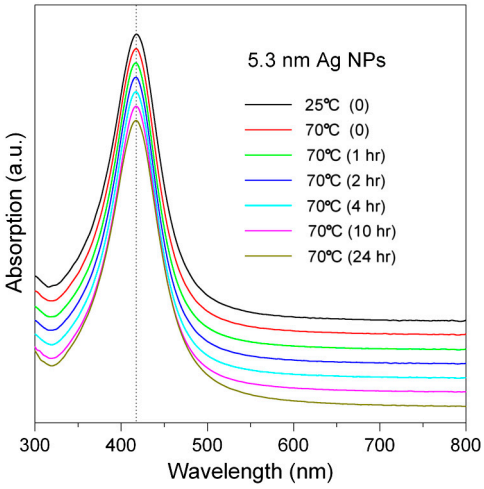

Fig. S7. Absorption spectra of a toluene dispersion of 5.3-nm Ag NPs before and after it was heated at 70 °C for different times. Air was bubbled throughout the heating process. The numbers in parentheses indicate the time relative to the time at which the temperature reached 70 °C. The vertical dotted line highlights the peak positions. The results clearly shows that no peak shift occurred during heating, indicating the colloidal Ag NPs are stable from oxidation. The peak width also remains unchanged. (The spectra have been normalized and displaced from one another for clarity.)

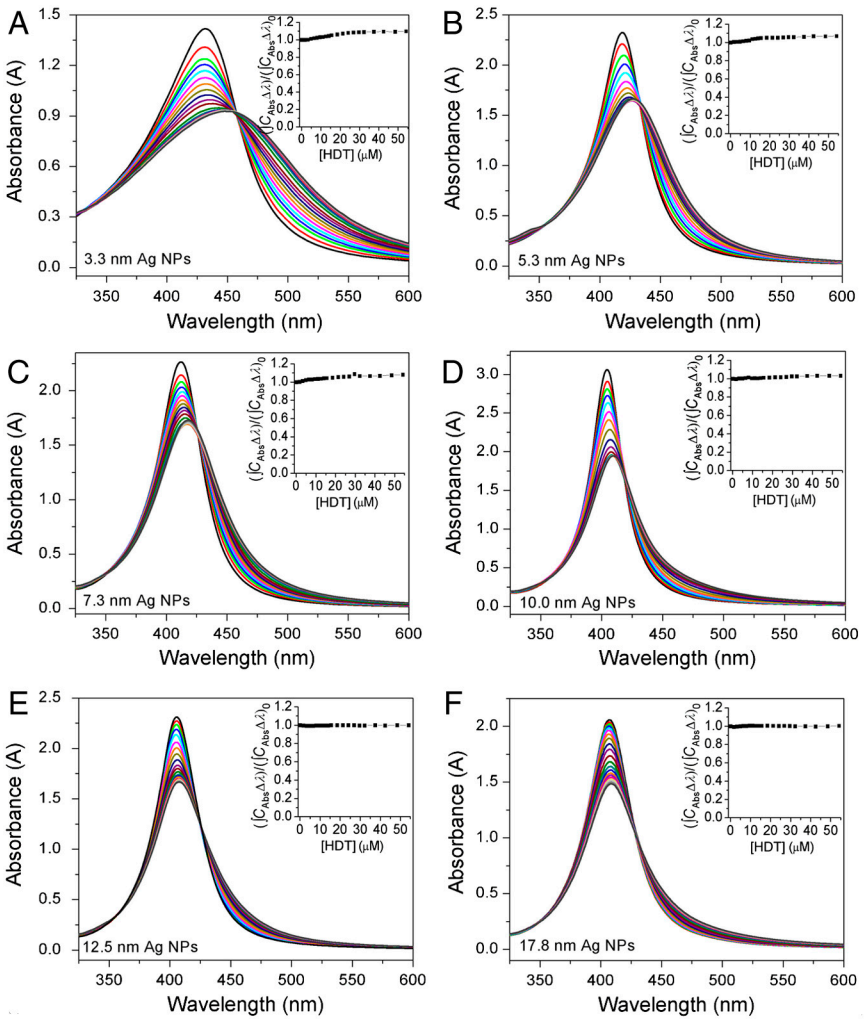

Fig. S8. Variation of the absorption spectra of the Ag NPs with different sizes upon titration with HDT. (*A*) 3.3 nm, (*B*) 5.3 nm, (*C*) 7.3 nm, (*D*) 10.0 nm, (*E*) 12.5 nm, and (*F*) 17.8 nm. The insets plot the integrated absorption peak area normalized against the initial area, $(\int C_{abs}\Delta\lambda)/(\int C_{abs}\Delta\lambda)_0$, as a function of [HDT].

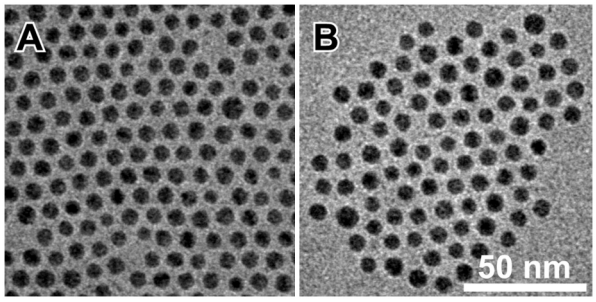

Fig. S9. Representative TEM images of 7.3-nm Ag NPs (*A*) before and (*B*) after surface ligand exchange using HDT molecules. The scale bar in *B* applies for both *A* and *B*.

Peng et al. www.pnas.org/cgi/doi/10.1073/pnas.1007524107

Table S1. Detailed parameters of the Ag NPs quantitatively calculated according to the absorption spectra and ICP-OES measurements

Average diameter of Ag NPs, d (nm)	Ag (wt%)in dry samples	Mass of the Ag core of a single NP ($\times 10^{-20}$ g)*	Particle numbers in 20 μg sample ($\times 10^{11}$)†	Absorbance at peak max. $A_{\lambda\text{-max}}$ from 20 μg NPs in 2 mL hexane (A)	Absorption cross section at peak max. for a single NP, $C_{\text{abs-max}}$ (nm^2)‡	Integrated absorption cross section (320–600 nm) for a single NP, $\int C_{\text{abs}} \Delta\lambda$ ($\times 10^2$ nm^3)
2.2	59.75	5.854	2041	0.307	0.7065	1.108
3.3	78.50	19.76	794.6	0.651	3.774	4.116
3.9	87.75	32.61	538.1	0.714	6.109	6.246
4.7	86.88	57.08	304.4	0.862	13.04	10.89
5.3	89.63	81.85	219.0	1.32	27.70	18.31
7.3	95.25	213.9	89.07	1.23	63.37	38.34
10.0	94.90	549.8	34.52	1.34	179.2	110.5
12.5	86.25	1074	16.06	1.38	394.5	238.2
15.6	96.70	2087	9.266	1.23	613.1	334.9
17.8	93.30	3101	6.018	1.21	923.1	603.8

*$m_{\text{Ag NP}} = \rho \cdot V_{\text{Ag NP}} = (1/6 \times 10^{-21}) \cdot \rho \cdot \pi d^3$, $m_{\text{Ag NP}}$ (g) is the weight of the inorganic core of a single NP, ρ (g/cm^3) is the density of silver (using bulk density 10.49 g/cm^3 here), $V_{\text{Ag NP}}$ (cm^3) is the volume of the inorganic core of the NP, d (nm) is TEM determined average diameter;

†$N_{20\ \mu\text{g NP}} = (20 \times 10^{-6}\ \text{g})(\text{Ag wt\%})/(m_{\text{Ag NP}})$, $N_{20\ \mu\text{g NP}}$ is the number of NPs per 20 μg, (Ag wt%) is the ICP determined weight percentage of inorganic silver in Ag NPs;

‡$C_{\text{abs-max}} = 2303\varepsilon_{\lambda\text{-max}}/N_A\ (\text{cm}^2) = 2303A_{\lambda\text{-max}}/c \cdot l \cdot N_A(\text{cm}^2) = 2303(A_{\lambda\text{-max}} \cdot V_{\text{soln}})/(N_{20\ \mu\text{g NP}} \cdot l)(\text{cm}^2) = 4.606A_{\lambda\text{-max}}/N_{20\ \mu\text{g NP}}(\text{cm}^2) = 4.606 \times 10^{14} \cdot A_{\lambda\text{-max}}/N_{20\ \mu\text{g NP}}(\text{nm}^2)$, (12). $C_{\text{abs-max}}$ (nm^2) is the absorption cross section at peak maximum, $\varepsilon_{\lambda\text{-max}}$ (M^{-1} cm^{-1}) is the extinction coefficient and equals $A_{\lambda\text{-max}}/c \cdot l$ according to Beer's Law, N_A is the Avogadro's number, $A_{\lambda\text{-max}}$ (A) is the maximum absorbance from the dispersion of 20 μg NPs in 2.0 mL hexane, c (M) is the particle concentration and equals $N_{20\ \mu\text{g NP}}/(V_{\text{soln}} \cdot N_A)$, V_{soln} (liter) is the overall solution volume and equals 2.0×10^{-3} liter, l (cm) is the path length of the incident light and equals 1 cm.